

Emergent topology by Landau level mixing in quantum Hall-superconductor nanostructures

Yuriko Baba ^{1,2,*}, Alfredo Levy Yeyati ^{1,2,3,†} and Pablo Bursat ^{1,2,3,‡}

¹*Department of Theoretical Condensed Matter Physics, Universidad Autónoma de Madrid, 28049 Madrid, Spain*

²*Condensed Matter Physics Center (IFIMAC), Universidad Autónoma de Madrid, 28049 Madrid, Spain*

³*Instituto Nicolás Cabrera, Universidad Autónoma de Madrid, 28049 Madrid, Spain*

(Dated: July 21, 2025)

We demonstrate the emergence of novel topological phases in quantum Hall-superconductor hybrid systems driven by Landau level mixing and spin-orbit interactions. Focusing on a narrow superconducting stripe atop a two-dimensional electron gas, we identify regimes where the hybridization of the chiral Andreev states at each side of the stripe leads to different phases beyond the long sought p -wave superconducting one. These topological phases exhibit distinctive transport signatures, including quantized nonlocal conductance arising from electron cotunneling at filling factor $\nu = 1$, which can coexist with quantized crossed Andreev reflection at $\nu = 2$. A combination of numerical simulations and effective modelling reveals the role of spin-orbit coupling and stripe geometry in controlling these transitions. Our findings suggest new strategies for realizing and detecting topology in proximized quantum Hall devices.

Introduction.— Quantum Hall (QH)-superconductor (SC) hybrid structures provide an attractive platform in the search of engineered topological phases [1–3]. In particular, p -wave topological superconductivity is expected to arise when two counter-propagating spin-polarized edge modes are coupled by a conventional SC [3–6].

While these proposals are based on idealized conditions, recent experimental progress in realizing proximized QH devices [7–18] has boosted theoretical investigations beyond early models [19–22]. These studies explore the influence of the interface transparency [23], disorder [24–27], device geometry [28–30], magnetic field penetration [6, 31], the effect of vortices [25, 32–34], or heat transport [35]. Additionally, other transport signatures like shot noise have been explored [36, 37]. Despite this progress, a definitive experimental confirmation of the presence of topological superconductivity in QH devices is lacking.

In this work we consider a setup where a narrow superconducting finger is placed on top of a Hall bar geometry defined on a two dimensional electron gas (2DEG), see Fig. 1(a). As discussed in Refs. [1, 5, 6], topological superconductivity emerges for $\nu = 1$ when the finger width W_S is comparable to the superconducting coherence length forming Majorana zero modes at its top and bottom terminations. In a nonlocal transport configuration like the one in Fig. 1(a), topological superconductivity would manifest in perfect crossed Andreev reflection (CAR), i.e., perfect electron-hole conversion as depicted in panel (i) of Fig. 1(b). By contrast, outside the topological phase no such quantization is expected and the nonlocal conductance $G_{nl} = (e^2/h)(T_{EC} - T_{CAR})$ could take any value (positive or negative), as a result of the competition between CAR and electron cotunneling (EC) processes.

We demonstrate that other previously unnoticed topological phases, with drastically different transport prop-

erties, can arise for QH-SC hybrid systems. These phases feature quantized transport channels with perfect EC and emerge when spin-orbit coupling dominates over Zeeman splitting and for pairs of Landau Levels (LLs) with an energy separation comparable to the superconducting gap.

A schematic phase diagram for an infinitely long SC stripe with periodic boundary conditions along the y direction is presented in Fig. 1(b). Pairs of electron and hole LLs at each edge of the stripe form chiral Andreev edge states (CAESs) and the inter-edge hybridization between them defines a set of subbands as a function of the parallel momentum k_y . When the chemical potential μ approaches the boundary between adjacent filling factors, and depending on the stripe width W_S , a band inversion can occur marked by a sign change in the associated Pfaffian invariant Q_S . In those regions [brighter areas in Fig. 1(b)] and for $\nu = 1$, the nonlocal conductance

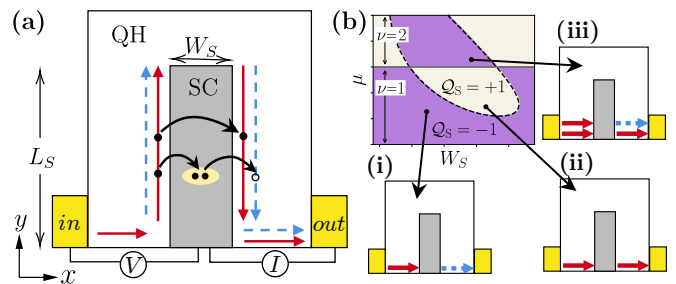


FIG. 1. (a) Sketch of a 2DEG in the QH regime with a superconducting finger of width W_S placed on top. Solid red and dashed blue arrows respectively represent electron and hole edge states coupled by the SC (gray). In a nonlocal transport measurement, voltage is applied between lead *in* and SC and current is measured in lead *out*. (b) Schematic phase diagram in the $\mu - W_S$ plane for an infinite SC stripe. Panels (i-iii) indicate the dominant transport processes in each region of the phase diagram for a finite-length SC finger.

in the finger geometry would jump to a quantized *positive* value, leading to perfect EC transmission [panel (ii)]. Remarkably, when increasing μ to reach $\nu = 2$ within these regions, the nonlocal conductance completely vanishes due to the opposite quantized contributions by EC and CAR processes corresponding to the two edge modes [panel (iii)].

In the first part of this work we analyze the phase diagram in terms of relevant parameters for the stripe geometry. We combine numerical calculations with an effective analytical model which allows us to get a simple physical picture of the origin of the different topological phases. We then present results for the transport properties which confirm the expected quantization for each phase, as well as their robustness against several factors.

Model and phase diagram analysis.— The system considered is a proximized 2DEG in the QH regime controlled by a perpendicular magnetic field B_z . The corresponding model Hamiltonian can be expressed as

$$\mathcal{H} = \left(\frac{\hbar^2 \mathbf{k}^2}{2m} - \mu(\mathbf{r}) \right) \sigma_0 \tau_z + V_z(\mathbf{r}) \sigma_z \tau_0 + \alpha_R(\mathbf{r}) (k_x \sigma_y \tau_0 - k_y \sigma_x \tau_0) - \Delta(\mathbf{r}) \tau_x \sigma_z, \quad (1)$$

where $\mathbf{k} = -i\nabla_{\mathbf{r}}$, while σ_j and τ_j , with $j = x, y, z$, are Pauli matrices corresponding to the spin and electron-hole spaces, respectively. The orbital part of the magnetic field is included by the minimal substitution $\hbar\mathbf{k} \rightarrow \hbar\mathbf{k} - q\mathbf{A}(\mathbf{r})$, where $\mathbf{A}(\mathbf{r})$ is the vector potential. This model includes the Rashba spin-orbit coupling (RSOC) through the $\alpha_R(\mathbf{r})$ term, the proximity-induced s -wave pairing ($\Delta(\mathbf{r})$ term) and the Zeeman splitting $V_z(\mathbf{r}) = g\mu_B B_z(\mathbf{r})/2$. We consider the RSOC to be constant throughout the device and the magnetic field to be exponentially suppressed inside the SC region with a characteristic decay length λ_B , see Supplemental Material [38] for more details on the model. In the following, we employ parameters which roughly correspond to 2DEG devices as the ones explored in Refs. [16, 17].

First, we analyze the topological phases in the stripe geometry already mentioned in the introduction (periodic in the y direction). For two decoupled interfaces (i.e., in the limit $W_S \gg \xi_S$, where ξ_S is the SC coherence length), the spectrum is gapless since the left (L) and right (R) CAESs exhibit a linear dispersion inside the SC gap Δ and do not hybridize; see Fig. 2(a). When the SC region is narrowed, the CAESs form hybridized subbands with a non-zero minigap E_g [Fig. 2(c-e)]. Depending on the width W_S of the SC stripe and on the chemical potential μ , the spectrum shows different topological phases determined by the invariant \mathcal{Q}_S that signals the topological superconducting phase for $\mathcal{Q}_S < 0$. The topological invariant is defined as

$$\mathcal{Q}_S = \text{sign} \left\{ \frac{\text{Pf}[\mathcal{A}(k_y = 0)]}{\text{Pf}[\mathcal{A}(k_y = \pi/a)]} \right\} (-1)^{-\nu}, \quad (2)$$

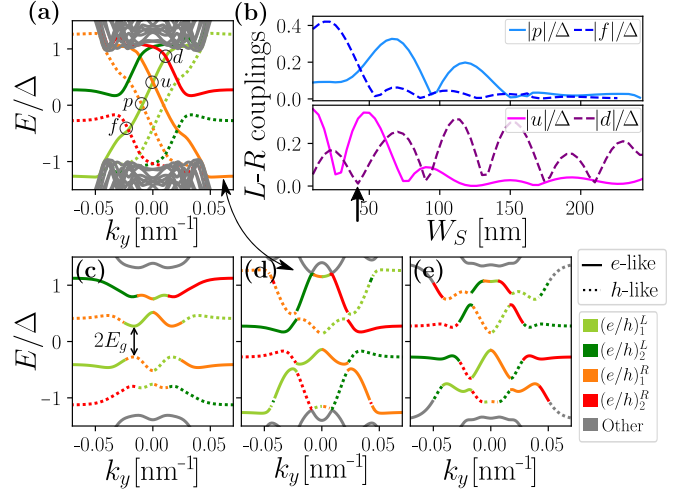


FIG. 2. Band dispersion in the stripe geometry with periodic boundary conditions along y for (a) uncoupled interfaces ($W_S \gg \xi_S$) with $\mu/\Delta = 2.1$ and (c, d, e) for $W_S = 48$ nm with, respectively, $\mu/\Delta = 1.2, 2.1, 2.6$. The colours indicate the projection over the CAESs in (a). (b) Effective couplings in (a) as a function of W_S for $\mu/\Delta = 2.1$.

where ν is the filling factor, a is the lattice constant used in the tight-binding discretization [38], and $\mathcal{A}(k_y) = H(k_y)U_C$ is a skew-symmetric matrix at the time-reversal invariant momenta [39–41], with U_C obtained from the particle-hole symmetry $\mathcal{C} = U_C\mathcal{K}$ (\mathcal{K} being the conjugation operator). The Pfaffian factor in Eq. (2) counts the total parity of the number of crossings between different subbands at the Fermi level in half of the Brillouin zone, i.e., for $k_y \in [0, \pi/a]$. On the other hand, the factor $(-1)^\nu$ removes the contribution from the edge states localized at the outer edge of the stripe, not in proximity to the SC [42], see End Matter. This way, \mathcal{Q}_S only takes into account the CAESs crossings, such that $\mathcal{Q}_S < 0$ indicates topological superconductivity on the stripe.

The coupling scheme between L and R states is particularly simple for filling factor $\nu = 1$, since only one pair of CAESs crosses the Fermi energy. In this regime one can obtain analytical insight from an *effective model* in terms of the lowest energy CAESs, see Eq. (8) in End Matter. Let us denote e_ν^S (h_ν^S), with $\nu = 1, 2$, the CAES obtained from the electron (hole) LLs localized at the side $S = L, R$. In terms of these states we express the Pfaffian invariant of the effective model as

$$\mathcal{Q}_S = (-1)^\nu \text{sign} \left[d^4 - 2d^2 (E_u E_d + p^2 + u^2) + (E_d^2 + p^2 - u^2) (E_u^2 + p^2 - u^2) \right], \quad (3)$$

where u , p , and d respectively denote the coupling terms $\langle e_1^L | \mathcal{H} | e_1^R \rangle$, $\langle e_1^L | \mathcal{H} | h_1^R \rangle$, and $\langle e_1^L | \mathcal{H} | e_2^R \rangle$, indicated by the circles in Fig. 2(a); whereas E_u and E_d correspond to the energy crossings for $W_S \gg \xi_S$. Notice, in particular, that p gives the size of the nonlocal p -wave coupling and u is related to EC processes connecting equal CAESs

localized at the two opposite interfaces. These coupling terms are calculated using a numerical projection on the uncoupled interface CAESs, i.e., the ones obtained in the limit of $W_S \gg \xi_S$. We represent them in Fig. 2(b) as a function of W_S . The couplings depend on W_S according to an exponential decay given by ξ_S and an oscillatory function of the Fermi wavevector k_F [6, 38]. The coupling term $f = \langle e_1^L | \mathcal{H} | h_2^R \rangle$ is neglected in Eq. (3), since it is strongly suppressed except for widths W_S of the order of the localization of the LLs, as shown in Fig. 2(b).

The couplings' oscillatory behaviour results in an alternation of topological and trivial stripe phases as a function of the width W_S and chemical potential μ , according to the interplay of the different terms in Eq. (3). Still, having a sign change in Q_S at filling factor one (i.e., for $\mu < \hbar\omega/2 + V_z$, with $\omega = eB_z/m$) requires special conditions on the energy scales involved. The analysis of these conditions using the effective model gets particularly simple if we consider a case where $d = 0$, like the one indicated by the arrow in Fig. 2(b). Then, the change of sign in Q_S simply requires $E_u^2 < u^2 - p^2$, which can be understood as the competition between EC (u) and CAR (p) processes when E_u is sufficiently small. This crossing energy is controlled by the interplay between the Rashba splitting $E_R = \alpha_R \sqrt{2eB_z/\hbar}$ and the Zeeman exchange V_z , and we estimate the sign change to take place for $2\hbar\omega/3 - V_z \lesssim E_R \lesssim \hbar\omega$ [38].

Going beyond the effective model, one can analyze the system phase diagram by direct diagonalization, which also allows us to identify the main character of the subband states in the basis of the decoupled CAESs. This information is encoded in the colour code and line style of the bands plotted in Fig. 2(c-e), where each panel corresponds to a particular case regarding the Q_S and ν values, in accordance with the three cases discussed in Fig. 1(i-iii). At filling factor $\nu = 1$ in the SC topological regime ($Q_S = -1$) [Fig. 2(c)], the lowest energy subband is a mode coupling L and R states of the $\nu = 1$ LL with opposite e - h nature, i.e., e_1^L and h_1^R for positive momenta. Since the coupled CAESs have the same ν and hence equal spin texture, this subband inversion is associated to the emergence of p -wave superconductivity on the stripe, in line with the invariant calculation [1].

By contrast, for a topologically trivial SC state ($Q_S = 1$) and $\nu = 1$ [Fig. 2(d)], a band inversion at zero momentum leads to a subband coupling filled electron state e_1^L and empty hole h_2^R such that Andreev conversion is prohibited. Even though $Q_S = 1$, the system maintains the QH topology that manifests in a quantized EC conductance for a finger SC, as we show below. Importantly, increasing the chemical potential to reach a higher filling factor $\nu = 2$ yields a sign change in the topological invariant, $Q_S = -1$. This $\nu = 2$ state now features two channels with different nontrivial topology [Fig. 2(e)]. One of the subbands is still inverted at zero momentum, with a prohibited coupling between e_1^L and h_1^R , leading again to

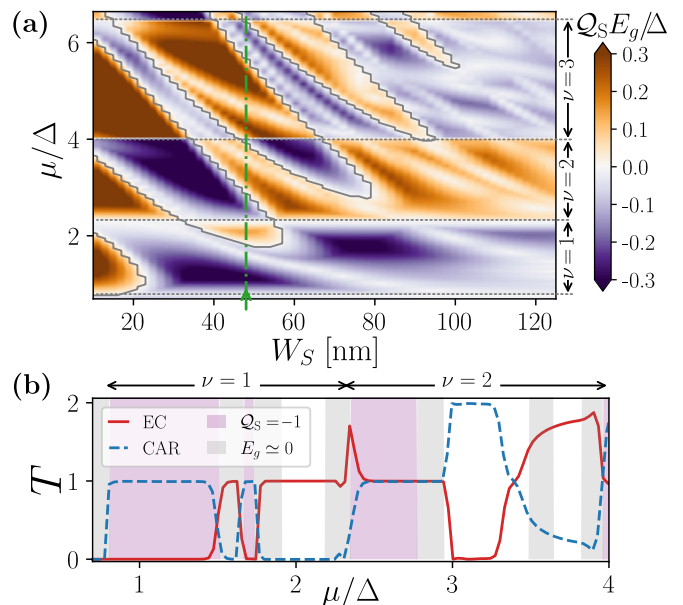


FIG. 3. (a) $W_S - \mu$ map of the product of minigap and invariant, $Q_S E_g$, for a stripe geometry with parameters in Table I. (b) Transmission probabilities for CAR and EC processes in a finger geometry of $W_S = 48$ nm [green line in (a)] and $L_S = 500$ nm. The energy of injection is $E_{\text{inj}}/\Delta = 10^{-3}$, see [38] for details on the transport calculations. The purple (grey) areas correspond to the $Q_S = -1$ (gapless) regions of a stripe geometry with the same W_S and periodic boundary conditions in the y direction.

a perfectly quantized EC process for the finger SC. By contrast, the now occupied second LL supports a nontrivial e - h coupling that leads to the subband inversion that restores p -wave superconductivity for the other channel.

The full phase diagram for the stripe geometry, calculated numerically with the set of parameters indicated in Table I of the End Matter, is shown in Fig. 3(a). In this figure, we plot $Q_S E_g$ as a function of μ and W_S . Notice that not all the gapless lines are associated to topological transitions since E_g also vanishes due to the oscillatory behaviour of the effective pairing between left-right CAESs. The actual topological transitions are indicated by the full grey lines, while the dashed horizontal lines indicate the changes in filling factor. As can be observed, the full grey lines define tilted tongue-like regions which widen as μ increases. These results correspond to the case of a significant RSOC ($\alpha = 20$ meV nm) and a rather small field ($B = 2.2$ T). As the spin-orbit coupling is reduced the tongue-like regions move towards higher μ values, eventually above the $\nu = 1$ line; whereas for higher fields these regions shrink (Fig. 8 in End Matter).

Transport properties.— The different topological phases identified earlier have a distinct and quantized transport signal for a finite SC finger geometry. In Fig. 3(b) the zero-energy transmission probabilities for the EC (T_{EC} , red line) and CAR (T_{CAR} , blue line)

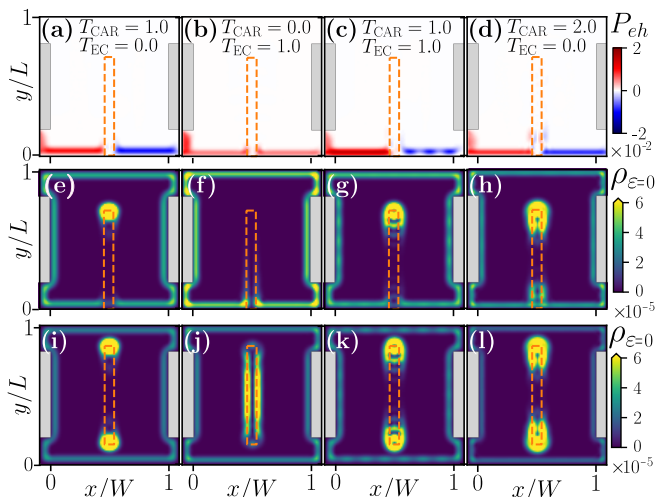


FIG. 4. Scattering wavefunction and local density of states for representative cases with $W_S = 48$ nm, $L_S = 500$ nm and total system size $W = 600$ nm \times $L = 700$ nm (the injection scheme is sketched in Fig. 1(a)). The columns correspond to $\mu/\Delta = \{1.2, 2.1, 2.6, 3.2\}$. (a-d) Electron and hole content $P_{eh}(\mathbf{r}) = |\psi_s^e(\mathbf{r})|^2 - |\psi_s^h(\mathbf{r})|^2$ of the scattering wavefunction ψ_s for an incoming electron at $E_{inj}/\Delta = 10^{-3}$; (e-l) local density of states at $\varepsilon = 0$ for the finger (e-h) and SC island configurations (i-l).

processes are calculated as a function of the chemical potential μ for a finite-finger configuration with fixed $W_S \times L_S$ [38, 43]. The gray and purple areas respectively mark the values of μ where the stripe configuration with the same W_S exhibits a gapless spectrum (gray) or an invariant $\mathcal{Q}_S = -1$ (purple).

For the values of μ with a non-zero minigap in the stripe, the nonlocal conductance G_{nl} is either quantized or zero. Indeed, for the topologically protected states with $\mathcal{Q}_S = -1$, the $\nu = 1$ channel is quantized featuring perfect CAR ($T_{CAR} = 1$). By contrast, the $\nu = 1$ mode with $\mathcal{Q}_S = +1$, where the band inversion prohibits the Andreev conversion, leads to $T_{EC} = 1$. Interestingly, for filling factor $\nu = 2$ the two previous channels coexist when $\mathcal{Q}_S = -1$, resulting in zero nonlocal conductance as the quantized EC and CAR contributions mutually cancel. On the other hand, for the states with $E_g \simeq 0$ in the stripe, we obtain a fragile or not even quantized G_{nl} that strongly depends on the length L_S of the finger and on the energy of injection E_{inj} . The transport results discussed in Fig. 3(b) remain qualitatively the same for different widths W_S and chemical potentials μ , as shown in Fig. 9(b) of End Matter.

As discussed above, the quantized CAR signal corresponds to the formation of pairs of Majorana modes at both ends of the finger, the lower one merging with the QH edge channel. To visualize the delocalization of this Majorana state into the CAES channel, in Fig. 4 we compare the electron-hole content of the scattering wavefunc-

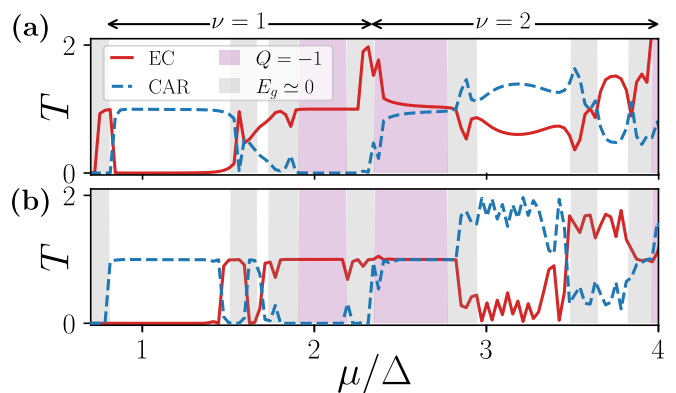


FIG. 5. Transmission probabilities for the case of Fig. 3(b) with (a) $E_{inj}/\Delta = 0.05$ and (b) $E_{inj}/\Delta = 10^{-3}$ and including Anderson disorder with on-site strength $w_A/\Delta = 10$ over an extension of 50 nm around the SC interface.

tions P_{eh} (top panels) with the local density of states at zero energy $\rho_{\varepsilon=0}$ for the finger configuration (middle panels) and for the case of a floating SC island detached from both sides of the QH edges (bottom panels).

For $\mathcal{Q}_S = -1$ a pair of localized Majorana states emerge at $\nu = 1$ [Fig. 4(i)] and $\nu = 2$ [Fig. 4(k)], in correspondence with the $T_{CAR} = 1$ channels shown in, respectively, Fig. 4(a) and Fig. 4(c). The important difference being that at $\nu = 2$ the CAR channel coexists with another perfectly quantized EC channel. When $\mathcal{Q}_S = 1$ we also have different behaviour depending on the filling factor. At $\nu = 1$, no localized states at the tips of the SC island are observed in Fig. 4(j). Indeed, the scattering wavefunction [Fig. 4(b)] and the local density of states [Fig. 4(f,j)] feature a channel that directly connects the LLs through the SC region. By contrast, at $\nu = 2$ there are two Majorana modes at the ends of the SC [Fig. 4(l)], leading to two quantized CAR channels in Fig. 4(d).

As indicated by the invariant \mathcal{Q}_S , the Majorana states are only topologically protected when an odd number of pairs emerge separated by $L_S \gg \xi_S$. For an even number, the zero-energy states form so-called *fragile* Majorana pairs that can be easily gapped [41]. We have verified this, as well as the robustness of the quantized transport signal to both changes in the injection energy and disorder from an on-site Anderson disorder in a region around the SC finger. As shown in Fig. 5, the values of μ corresponding to a topological state, i.e., when $\mathcal{Q}_S = -1$ for both filling factors and $T_{EC} = 1$ for $\nu = 1$, are particularly stable to both perturbations. By contrast, the CAR signal for two pairs of Majorana states is indeed highly sensitive to both disorder and changes in the injection energy. Similarly, the transmission for gapless regions is also highly sensitive to perturbations.

Conclusions.— Our work reveals the existence of unconventional topological phases marked by quantized EC nonlocal conductance in proximized 2DEG devices in the

QH state. We have confirmed the robustness of these phases by numerical simulations using parameters representative of recent experiments [16, 17]. We have focused on the lowest filling factors in order to simplify the theoretical analysis and found that the topological phases displaying perfect EC emerge at low fields and large spin-orbit splitting. Although reaching $\nu = 1, 2$ in these conditions might be experimentally demanding, the emergent phases are also present at higher filling factors [see Fig. 3(a)] which can be within reach using state of the art techniques.

Acknowledgments.— We thank R. Sánchez, L. Arachea, C. Balseiro and A. R. Akhmerov for valuable discussions. The work was supported by Spanish CM “Talento Program” project No. 2019-T1/IND-14088 and No. 2023-5A/IND-28927, the Agencia Estatal de Investigación project No. PID2020-117992GA-I00, No. CNS2022-135950 and No. PID2023-150224NB-I00 and through the “María de Maeztu” Programme for Units of Excellence in R&D (CEX2023-001316-M).

* yuriko.baba@uam.es

† a.l.yeyati@uam.es

‡ pablo.burset@uam.es

- [1] D. J. Clarke, J. Alicea, and K. Shtengel, Exotic circuit elements from zero-modes in hybrid superconductor-quantum-Hall systems, *Nature Physics* **10**, 877 (2014).
- [2] R. S. K. Mong, D. J. Clarke, J. Alicea, N. H. Lindner, P. Fendley, C. Nayak, Y. Oreg, A. Stern, E. Berg, K. Shtengel, and M. P. A. Fisher, Universal topological quantum computation from a superconductor-Abelian quantum Hall heterostructure, *Physical Review X* **4**, 011036 (2014).
- [3] X.-L. Qi, T. L. Hughes, and S.-C. Zhang, Chiral topological superconductor from the quantum Hall state, *Physical Review B* **82**, 184516 (2010).
- [4] L. Fu and C. L. Kane, Superconducting proximity effect and Majorana fermions at the surface of a topological insulator, *Phys. Rev. Lett.* **100**, 096407 (2008).
- [5] F. Finocchiaro, F. Guinea, and P. San-Jose, Topological π junctions from crossed Andreev reflection in the quantum Hall regime, *Physical Review Letters* **120**, 116801 (2018).
- [6] T. H. Galambos, F. Ronetti, B. Hetényi, D. Loss, and J. Klinovaja, Crossed Andreev reflection in spin-polarized chiral edge states due to the Meissner effect, *Physical Review B* **106**, 075410 (2022).
- [7] F. Amet, C. T. Ke, I. V. Borzenets, J. Wang, K. Watanabe, T. Taniguchi, R. S. Deacon, M. Yamamoto, Y. Bomze, S. Tarucha, and G. Finkelstein, Supercurrent in the quantum Hall regime, *Science* **352**, 966 (2016).
- [8] G.-H. Park, M. Kim, K. Watanabe, T. Taniguchi, and H.-J. Lee, Propagation of superconducting coherence via chiral quantum-Hall edge channels, *Scientific Reports* **7**, 10.1038/s41598-017-11209-w (2017).
- [9] G.-H. Lee, K.-F. Huang, D. K. Efetov, D. S. Wei, S. Hart, T. Taniguchi, K. Watanabe, A. Yacoby, and P. Kim, Inducing superconducting correlation in quantum Hall edge states, *Nature Physics* **13**, 693 (2017).
- [10] M. T. Wei, A. W. Draelos, A. Seredinski, C. T. Ke, H. Li, Y. Mehta, K. Watanabe, T. Taniguchi, M. Yamamoto, S. Tarucha, G. Finkelstein, F. Amet, and I. V. Borzenets, Chiral quasiparticle tunneling between quantum Hall edges in proximity with a superconductor, *Physical Review B* **100**, 121403 (2019).
- [11] A. Seredinski, A. W. Draelos, E. G. Arnault, M.-T. Wei, H. Li, T. Fleming, K. Watanabe, T. Taniguchi, F. Amet, and G. Finkelstein, Quantum Hall-based superconducting interference device, *Science Advances* **5**, 10.1126/sciadv.aaw8693 (2019).
- [12] M. R. Sahu, A. K. Paul, J. Sutradhar, K. Watanabe, T. Taniguchi, V. Singh, S. Mukerjee, S. Banerjee, and A. Das, Quantized conductance with nonzero shot noise as a signature of Andreev edge state, *Physical Review B* **104**, 1081404 (2021).
- [13] O. Gül, Y. Ronen, S. Y. Lee, H. Shapourian, J. Zauberman, Y. H. Lee, K. Watanabe, T. Taniguchi, A. Vishwanath, A. Yacoby, and P. Kim, Andreev reflection in the fractional quantum Hall state, *Physical Review X* **12**, 021057 (2022).
- [14] L. Zhao, Z. Iftikhar, T. F. Q. Larson, E. G. Arnault, K. Watanabe, T. Taniguchi, F. Amet, and G. Finkelstein, Loss and decoherence at the quantum Hall-superconductor interface, *Physical Review Letters* **131**, 176604 (2023).
- [15] H. Vignaud, D. Perconte, W. Yang, B. Kousar, E. Wagner, F. Gay, K. Watanabe, T. Taniguchi, H. Courtois, Z. Han, H. Sellier, and B. Sacépé, Evidence for chiral supercurrent in quantum Hall Josephson junctions, *Nature* **624**, 545 (2023).
- [16] M. Hatefipour, J. J. Cuozzo, J. Kanter, W. M. Strickland, C. R. Allemang, T.-M. Lu, E. Rossi, and J. Shabani, Induced superconducting pairing in integer quantum Hall edge states, *Nano Letters* **22**, 6173 (2023).
- [17] M. Hatefipour, J. J. Cuozzo, I. Levy, W. M. Strickland, D. Langone, E. Rossi, and J. Shabani, Andreev reflection of quantum Hall states through a quantum point contact, *Physical Review B* **109**, 035430 (2024).
- [18] T. Akiho, H. Irie, Y. Nakazawa, S. Sasaki, N. Kumada, and K. Muraki, Andreev reflection in the quantum Hall regime at an Al/InAs junction on a cleaved edge, *Nano Letters* **24**, 14790 (2024).
- [19] H. Hoppe, U. Zülicke, and G. Schön, Andreev reflection in strong magnetic fields, *Physical Review Letters* **84**, 1804 (2000).
- [20] F. Giazotto, M. Governale, U. Zülicke, and F. Beltram, Andreev reflection and cyclotron motion at superconductor—normal-metal interfaces, *Physical Review B* **72**, 054518 (2005).
- [21] A. R. Akhmerov and C. W. J. Beenakker, Detection of valley polarization in graphene by a superconducting contact, *Physical Review Letters* **98**, 157003 (2007).
- [22] I. M. Khaymovich, N. M. Chtchelkatchev, I. A. Shereshevskii, and A. S. Mel’nikov, Andreev transport in two-dimensional normal-superconducting systems in strong magnetic fields, *EPL (Europhysics Letters)* **91**, 17005 (2010).
- [23] A. Bondarev, G. Zhang, and H. U. Baranger, Transparent graphene-superconductor interfaces: Quantum Hall and zero field regimes, *Phys. Rev. B* **111**, 235444 (2025).
- [24] A. Manesco, I. M. Flór, C.-X. Liu, and A. Akhmerov, Mechanisms of Andreev reflection in quantum Hall graphene, *SciPost Physics Core* **5**, 10.21468/scipost-

- physcore.5.3.045 (2022).
- [25] V. D. Kurilovich, Z. M. Raines, and L. I. Glazman, Disorder-enabled Andreev reflection of a quantum Hall edge, *Nature Communications* **14**, 10.1038/s41467-023-37794-1 (2023).
- [26] V. D. Kurilovich and L. I. Glazman, Criticality in the crossed Andreev reflection of a quantum Hall edge, *Physical Review X* **13**, 031027 (2023).
- [27] J. J. Cuzzo and E. Rossi, SU(4) symmetry breaking and induced superconductivity in graphene quantum Hall edges, *Physical Review B* **110**, 024518 (2024).
- [28] A. David, J. S. Meyer, and M. Houzet, Geometrical effects on the downstream conductance in quantum-Hall–superconductor hybrid systems, *Physical Review B* **107**, 125416 (2023).
- [29] M. Beconcini, M. Polini, and F. Taddei, Nonlocal superconducting correlations in graphene in the quantum Hall regime, *Physical Review B* **97**, 201403 (2018).
- [30] V. Khrapai, Quantum Hall Bogoliubov interferometer, *Physical Review B* **107**, 1241401 (2023).
- [31] A. B. Michelsen, P. Recher, B. Braunecker, and T. L. Schmidt, Supercurrent-enabled Andreev reflection in a chiral quantum Hall edge state, *Physical Review Research* **5**, 013066 (2023).
- [32] B. Zocher and B. Rosenow, Topological superconductivity in quantum Hall–superconductor hybrid systems, *Physical Review B* **93**, 214504 (2016).
- [33] Y. Tang, C. Knapp, and J. Alicea, Vortex-enabled Andreev processes in quantum Hall–superconductor hybrids, *Physical Review B* **106**, 245411 (2022).
- [34] N. Schiller, B. A. Katzir, A. Stern, E. Berg, N. H. Lindner, and Y. Oreg, Superconductivity and fermionic dissipation in quantum Hall edges, *Physical Review B* **107**, 1161105 (2023).
- [35] C. Panu, F. Taddei, M. Polini, and A. Yacoby, Heat-charge separation in a hybrid superconducting quantum Hall setup, *Physical Review B* **110**, 1161407 (2024).
- [36] O. Gamayun, J. A. Hutasoit, and V. V. Cheianov, Two-terminal transport along a proximity-induced superconducting quantum Hall edge, *Physical Review B* **96**, 241104 (2017).
- [37] L. Arrachea, A. L. Yeyati, and C. A. Balseiro, Signatures of triplet superconductivity in $\nu=2$ chiral Andreev states, *Physical Review B* **109**, 064519 (2024).
- [38] See Supplemental Material, including Refs. [44, 45], where we provide further details about the model Hamiltonian, the effective analytical model, the finite-size effects in the finger and island geometry and on the variation of the phase diagrams with other parameters.
- [39] S. Tewari, T. D. Stanescu, J. D. Sau, and S. Das Sarma, Topological minigap in quasi-one-dimensional spin-orbit-coupled semiconductor Majorana wires, *Physical Review B* **86**, 024504 (2012).
- [40] M. Sato and Y. Ando, Topological superconductors: a review, *Reports on Progress in Physics* **80**, 076501 (2017).
- [41] D. Heffels, D. Burke, M. R. Connolly, P. Schüffegen, D. Grützmacher, and K. Moors, Robust and fragile Majorana bound states in proximitized topological insulator nanoribbons, *Nanomaterials* **13**, 723 (2023).
- [42] K. Shiozaki and M. Sato, Topology of crystalline insulators and superconductors, *Physical Review B* **90**, 165114 (2014).
- [43] C. W. Groth, M. Wimmer, A. R. Akhmerov, and X. Waintal, Kwant: a software package for quantum transport, *New Journal of Physics* **16**, 063065 (2014).
- [44] S.-Q. Shen, M. Ma, X. C. Xie, and F. C. Zhang, Resonant spin Hall conductance in two-dimensional electron systems with a Rashba interaction in a perpendicular magnetic field, *Physical Review Letters* **92**, 256603 (2004).
- [45] J. Schliemann, J. C. Egues, and D. Loss, Variational study of the $\nu = 1$ quantum Hall ferromagnet in the presence of spin-orbit interaction, *Physical Review B* **67**, 085302 (2003).
- [46] A. P. Schnyder, S. Ryu, A. Furusaki, and A. W. W. Ludwig, Classification of topological insulators and superconductors in three spatial dimensions, *Physical Review B* **78**, 195125 (2008).
- [47] S. Ryu, A. P. Schnyder, A. Furusaki, and A. W. W. Ludwig, Topological insulators and superconductors: tenfold way and dimensional hierarchy, *New Journal of Physics* **12**, 065010 (2010).
- [48] M. Wimmer, Algorithm 923: Efficient numerical computation of the Pfaffian for dense and banded skew-symmetric matrices, *ACM Transactions on Mathematical Software* **38**, 1 (2012).
- [49] C.-K. Chiu, J. C. Y. Teo, A. P. Schnyder, and S. Ryu, Classification of topological quantum matter with symmetries, *Reviews of Modern Physics* **88**, 035005 (2016).
- [50] S. Adachi, *Properties of Semiconductor Alloys: Group-IV, III–V and II–VI Semiconductors* (Wiley, 2009).
- [51] J. Yuan, M. Hatefipour, B. A. Magill, W. Mayer, M. C. Dartiailh, K. Sardashti, K. S. Wickramasinghe, G. A. Khodaparast, Y. H. Matsuda, Y. Kohama, Z. Yang, S. Thapa, C. J. Stanton, and J. Shabani, Experimental measurements of effective mass in near-surface InAs quantum wells, *Physical Review B* **101**, 205310 (2020).
- [52] N. Lotfizadeh, W. F. Schiela, B. Pekerten, P. Yu, B. H. Elfeky, W. M. Strickland, A. Matos-Abiague, and J. Shabani, Superconducting diode effect sign change in epitaxial Al-InAs Josephson junctions, *Communications Physics* **7**, 10.1038/s42005-024-01618-5 (2024).
- [53] K. S. Wickramasinghe, W. Mayer, J. Yuan, T. Nguyen, L. Jiao, V. Manucharyan, and J. Shabani, Transport properties of near surface InAs two-dimensional heterostructures, *Applied Physics Letters* **113**, 10.1063/1.5050413 (2018).
- [54] S. M. Farzaneh, M. Hatefipour, W. F. Schiela, N. Lotfizadeh, P. Yu, B. H. Elfeky, W. M. Strickland, A. Matos-Abiague, and J. Shabani, Observing magnetoanisotropic weak antilocalization in near-surface quantum wells, *Physical Review Research* **6**, 013039 (2024).
- [55] S. D. Escribano, A. Maiani, M. Leijnse, K. Flensberg, Y. Oreg, A. Levy Yeyati, E. Prada, and R. Seoane Souto, Semiconductor-ferromagnet-superconductor planar heterostructures for 1D topological superconductivity, *npj Quantum Materials* **7**, 10.1038/s41535-022-00489-9 (2022).

End Matter

Symmetry properties and topological invariant of the stripe system.— The Hamiltonian \mathcal{H} in Eq. (1), representing the proximized QH system, belongs in class D of the Altland-Zirnbauer classification due to the intrinsic particle-hole symmetry and broken time-reversal symmetry by the external magnetic field [42, 46, 47]. This phase is characterized, in 1D systems, by an invariant defined by the change of sign of the Pfaffian in the particle-symmetric momenta $k_y = 0, \pi/a$, where a skew-symmetric matrix can be obtained from the full-Hamiltonian. We define this invariant as [39–41]

$$\mathcal{Q}_T = \text{sign} \left\{ \text{Pf} [\mathcal{H}(k_y = 0)U_C] / \text{Pf} [\mathcal{H}(k_y = \pi/a)U_C] \right\}, \quad (4)$$

where $U_C = \tau_x \sigma_x$ is obtained from the particle-hole symmetry $\mathcal{C} = U_C \mathcal{K}$. \mathcal{Q}_T is calculated numerically using `Pfapack` [48].

The stripe geometry has a magnetic in-plane mirror reflection that works as an emergent time-reversal symmetry, reducing the D class to BDI. In fact, the in-plane reflection acts as

$$\mathcal{A}_x \mathcal{H}(k_y) \mathcal{A}_x^{-1} = \mathcal{H}(-k_y), \quad \mathcal{A}_x^2 = 1, \quad (5)$$

where $\mathcal{A}_x = \mathcal{M}_x \mathcal{K}$, with $\mathcal{M}_x = iP_x \tau_0 \sigma_z$ and P_x being the inversion operator $x \rightarrow -x$. Considering this emergent time-reversal symmetry, a chiral symmetry Γ is defined by the product of time-reversal and particle-hole leading to $\Gamma = -\tau_x \sigma_y$. In the basis that diagonalizes Γ , we can recast the stripe Hamiltonian as a two off-diagonal blocks $D(k_y)$ with winding number \mathcal{W} defined by [49]

$$\mathcal{W} = \int_{k=0}^{k=\frac{\pi}{a}} \frac{d\theta(k)}{\pi}, \quad \theta(k) = -i \ln \left[\frac{\det[D(k)]}{|\det[D(k)]|} \right]. \quad (6)$$

The Pfaffian invariant \mathcal{Q}_T is the parity of the winding number since $\mathcal{Q}_T = e^{i\pi\mathcal{W}}$.

To separate the contributions from the CAESs and the outer LLs, we split the integral in Eq. (6) as $\mathcal{W} = \mathcal{W}_{\text{CAES}} + \mathcal{W}_{\text{LL}}$, with $\mathcal{W}_{\text{CAES}} = \int_{k=0}^{k=k_{\text{LL}}} d\theta(k)/\pi$ and $\mathcal{W}_{\text{LL}} = \int_{k=k_{\text{LL}}}^{k=\pi/a} d\theta(k)/\pi$, where $k_{\text{LL}} > 0$ is the minimum (positive) momentum where the outer LL states cross the Fermi level. This way, we can separate the two contributions to the Pfaffian invariant as

$$\mathcal{Q}_T = \mathcal{Q}_S \mathcal{Q}_N, \quad \mathcal{Q}_S = e^{i\theta(k_{\text{LL}}) - i\theta(0)}, \quad \mathcal{Q}_N = (-1)^\nu, \quad (7)$$

where we have used that the Pfaffian of the outer LLs \mathcal{Q}_N is the parity of the filling factor. Figure 6 shows the winding phase as a function of the momenta for some representative cases.

Effective model for two lowest LLs.— The minimal model employed to describe the coupling of the CAESs

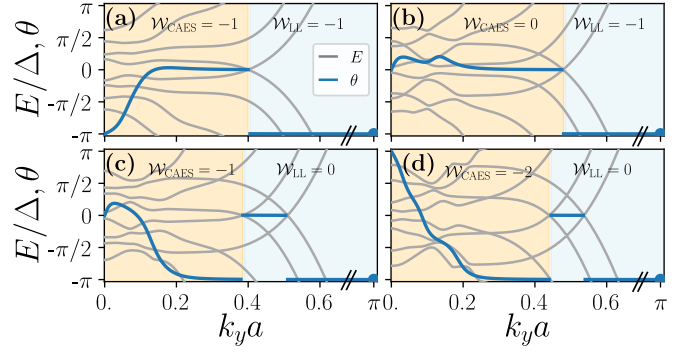


FIG. 6. Winding angle θ as a function of k_y in the stripe geometry. The parameters are the same as in Fig. 2 with fixed $W_S = 48$ nm and $\mu/\Delta = 1.2, 2.1, 2.6, 3.2$ for panels (a-d). The regions corresponding to the CAESs contributions and outer LLs are highlighted in orange and blue, respectively. As a reference, the dispersion relation is included in grey lines.

for $\nu = 1, 2$ states in the stripe geometry is

$$\begin{aligned} \mathcal{H}_{\text{eff}} = \sum_{k_y} \Psi_{k_y}^\dagger & \left[vk_y \tau_0 r_0 s_z + (E_u r_u + E_d r_d) \tau_z s_0 \right. \\ & + u \tau_0 r_z s_x + f \tau_x r_z s_0 \\ & \left. + (p \tau_x + d \tau_0) r_y s_y + M k_y^2 \tau_z r_0 s_0 \right] \Psi_{k_y}, \quad (8) \end{aligned}$$

with $\Psi_{k_y} = [c_{e2}^R, c_{e2}^L, c_{e1}^R, c_{e1}^L, (c_{h1}^R)^\dagger, (c_{h1}^L)^\dagger, (c_{h2}^R)^\dagger, (c_{h2}^L)^\dagger]^T$. Here, c_{it}^S annihilates an electron in the CAES of side $S = L, R$ obtained from the LL of type $t = e, h$ and index $\nu = 1, 2$; τ_i, r_i, s_i , with $i = 0, x, y, z$, are the identity and Pauli matrices respectively acting on the particle-hole space, the ν index, and the interface side; and $r_{d,u} = (r_0 \pm r_z)/2$.

In the effective model of Eq. (8), the CAESs are described by a linear dispersion with velocity v and with energy $E_{u(d)}$ at $k_y = 0$ for the CAES with $\nu = 1$ (2). The coupling terms considered connect CAESs localized at opposite sides of the SC. As defined in the manuscript, u (d) couples states with the same particle-hole nature and same (different) index ν . The coupling that mixes electron and hole states is given by p (f) for the same (different) ν . A quadratic correction proportional to M is considered to regularize the Dirac linear equation.

The topological invariant in Eq. (2) for the effective model is obtained analytically by evaluating the Pfaffian at $k_y = 0$, resulting in

$$\begin{aligned} \mathcal{Q}_S = (-1)^\nu & [d^4 + (f^2 + p^2 - u^2)^2 + E_u^2 E_d^2 \\ & + 2f^2(E_u E_d + f^2) - (E_d^2 + E_u^2)(u^2 - p^2) \\ & - 2d^2(E_u E_d + p^2 + u^2) - 4dfp(E_d - E_u)]. \quad (9) \end{aligned}$$

We can neglect f , which is strongly suppressed, to reach Eq. (3).

By considering the central stripe region as a superconducting Rashba-quantum well coupled to two QH regions

with well-defined LLs [38] the coupling terms can be expressed as [6]

$$c \approx c_0 \exp(-W_S/\xi_c) \cos(k_{F,c}W_S + \varphi_c), \quad (10)$$

for $c = u, p, d, f$, such that u_0, p_0, f_0 and d_0 are real constants with units of energy and φ_c takes the values $\varphi_p = \varphi_f = \pi/2$ and $\varphi_u = \varphi_d = 0$. The Fermi momentum is approximated by $k_{F,c} = \sqrt{2m_S(\mu_S + E_c)/\hbar^2 + 1/l_R^2}$, where E_c is the energy of the crossing point and $l_R = \hbar^2/(m\alpha)$. The decay length of the couplings inside the SC is also considered to be energy-dependent as $\xi_u = \xi_p = \xi_S, \xi_d \rightarrow \infty$ and $\xi_f = \xi_S/2$, where the SC coherence length at the Fermi level is given by $\xi_S = (\hbar/\Delta)\sqrt{2\mu/m_S}$.

We fix the initial amplitudes c_0 by considering only the spin structure of the LLs [38]. The couplings are then expressed as a function of the ratio of the Zeeman V_z and the Rashba E_R splitting,

$$\beta = (\hbar\omega/2 + V_Z)/\sqrt{(\hbar\omega/2 + V_Z)^2 + E_R^2},$$

as $u_0 \approx \Delta\beta, p_0 \approx \Delta\sqrt{1-\beta^2}, d_0 \approx \Delta\sqrt{(1-\beta)/2}, f_0 \approx \Delta\sqrt{(1+\beta)/2}$. In the absence of RSOC, $p_0 = d_0 = 0$.

Using these approximations, the W_S dependency of the coupling terms is computed in Fig. 7(a) for a fixed μ . The estimated values can be compared to the numerically computed projectors in Fig. 2(a). The phase diagram of the effective model is calculated in Fig. 7(b), showing a qualitative agreement with the complete calculation in Fig. 3(a).

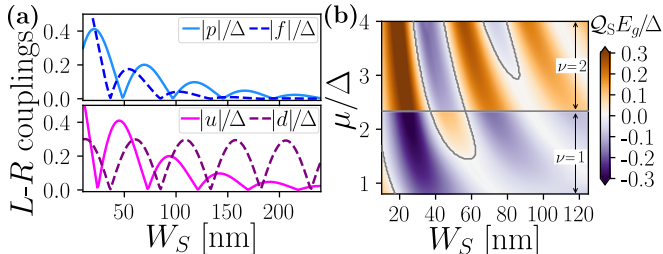


FIG. 7. Effective model. (a) Dependence of the coupling terms on W_S at fixed $\mu/\Delta = 2.1$. (b) Phase diagram for the region of $\nu = 1$ and $\nu = 2$. We estimate $E_u/\Delta = 0.35$, $E_d/\Delta = 1.1$, with the other parameters from Table I.

Comments on parameters.— The parameter values used in the plots of the main text are listed in Table I. They have been chosen to be representative of $\text{Ga}_x\text{In}_{1-x}\text{As}/\text{Nb}$ devices where the effective mass is estimated of the order of $m^* \approx 0.02 - 0.07m_e$ [50], the effective g -factor is $|g^*| \approx 10 - 15$ [51] and $\alpha_R \gtrsim 10$ meV nm [52] or even higher [53–55].

Phase diagrams for other sets of parameters are shown in Fig. 8. The resulting topological regions exhibit different extensions and appear at different values of μ and W_S depending on the RSOC and magnetic field when

$\Delta = 1$ meV,	$a = 2$ nm,	$m_{\text{eff}}/m_e \simeq 0.07$,	$B_z = 2.2$ T,
$\alpha_R = 20$ meV nm,	$g = -8$,	$\lambda_B = 6$ nm.	

TABLE I. Parameters for the main text calculations.

compared to Fig. 3(a). As can be observed in Fig. 8(a), using the same field as Fig. 3(a) but with smaller α_R , the lowest tongue-like region does not reach filling factor $\nu = 1$. At higher fields and lower RSOC [e.g., Fig. 8(c)] the tongue-like regions get narrower. The variation of the maps with other parameters is illustrated in Ref. [38].

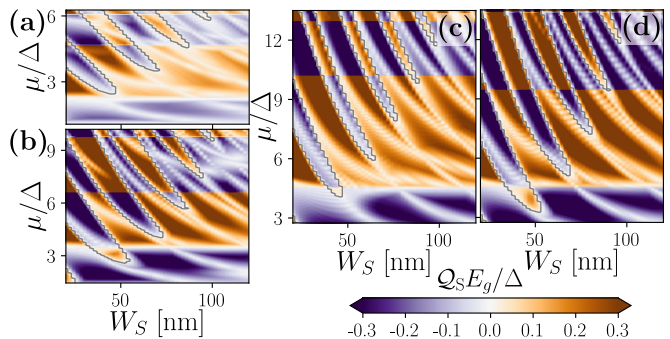


FIG. 8. Phase diagrams varying α_R and B_z . For panels (a-d) the RSOC and the magnetic field are respectively set to α_R [meV nm] = 10, 20, 10, 20 and B_z [T] = 2.2, 3.5, 5, 5.

Consistency between phase diagram, nonlocal conductance and Majorana number.— Figure 9 illustrates the consistency between the Q_S phase diagram for the stripe configuration (a) with the G_{nl} for the finger geometry (b), and the number \mathcal{N} of Majorana zero modes in the SC island (c).

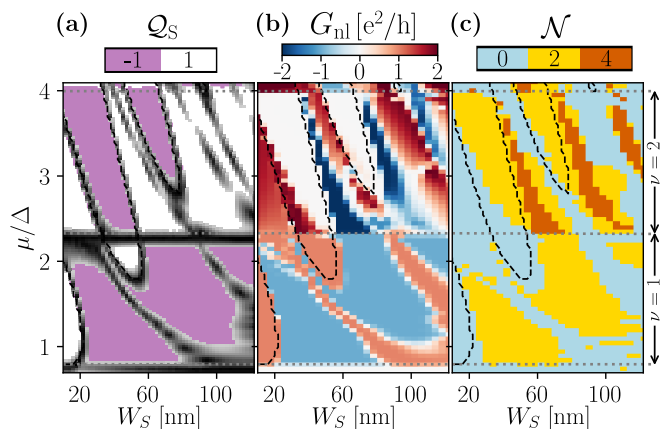


FIG. 9. (a) Phase diagram showing the Pfaffian invariant Q_S and the gapless regions (grey) for a stripe configuration. (b) Conductance G_{nl} in a finger geometry. (c) Number of Majorana zero modes \mathcal{N} in a SC island configuration. The parameters used are listed in Table I.

SUPPLEMENTAL MATERIAL TO “EMERGENT TOPOLOGY BY LANDAU LEVEL MIXING IN QUANTUM HALL-SUPERCONDUCTOR NANOSTRUCTURES”

In this supplemental material we provide further details on our model for a proximized 2DEG in the QH regime, including the spatial dependence assumed for all parameters and the discretization procedure used in the numerical calculations. We also describe the approximations considered for an analytical description of the phase diagrams within an effective model and discuss the finite-size effects on the transport properties in the finger and island geometries. Finally, we compute numerical phase diagrams for other sets of parameters than those considered in the main text.

DETAILS ON THE MODEL AND NUMERICAL CALCULATIONS

Model Hamiltonian.— As stated in the main text, the general Hamiltonian that we consider can be written as

$$\mathcal{H} = \left(\frac{\hbar^2 \mathbf{k}^2}{2m} - \mu(\mathbf{r}) \right) \sigma_0 \tau_z + V_z(\mathbf{r}) \sigma_z \tau_0 + \alpha_R(\mathbf{r}) (k_x \sigma_y \tau_0 - k_y \sigma_x \tau_0) - \Delta(\mathbf{r}) \tau_x \sigma_z, \quad (\text{S1})$$

where $\mathbf{k} = -i\nabla_{\mathbf{r}}$, while σ_i and τ_i are Pauli matrices and correspond to the spin and electron-hole space, respectively. All potentials defined in Eq. (S1) are space dependent. In this way, the proximized SC region can be conveniently defined by space-dependent functions. In the results presented in the main text, the RSOC $\alpha_R(\mathbf{r})$ is assumed to be constant all over the device and the Zeeman splitting V_z is assumed to decay in a Gaussian-like shape within the SC region as

$$V_z(\mathbf{r}) = \begin{cases} V_z^N, & \text{if } \mathbf{r} \in \text{N region,} \\ V_z^N \exp\left(-\frac{|\mathbf{r}-\mathbf{r}_{\text{NS}}|^2}{2\lambda_z^2}\right), & \text{if } \mathbf{r} \in \text{SC region,} \end{cases} \quad (\text{S2a})$$

where the vector $\mathbf{r}_{\text{NS}} = (x_{\text{NS}}, y_{\text{NS}})$ indicates the position of the nearest N-SC interface. The Zeeman splitting is given by the magnetic field as $V_z^N = g^* \mu_B B_z / 2$, where μ_B is the Bohr magneton and g^* is the effective g factor. The magnetic field is included via the vector potential, for which we choose the following gauge

$$\mathbf{A}(\mathbf{r}) = (0, A_y(x), 0), \quad \text{with } A_y(x) = \begin{cases} B_z(x - x_{\text{NS}} + \zeta_x \lambda_B), & \text{if } x \in \text{N region,} \\ \zeta_x B_z \lambda_B \exp\left(-\frac{|x-x_{\text{NS}}|}{\lambda_B}\right), & \text{if } x \in \text{SC region,} \end{cases}$$

where $\zeta_x = \text{sign}(x - x_{\text{NS}})$. In the finger geometry, the regions of fixed y without a SC interface are defined by the aforementioned $A_y(x)$ with $\zeta_x = 0$. The chemical potential is defined by

$$\mu(\mathbf{r}) = \begin{cases} \mu_N, & \text{if } \mathbf{r} \in \text{N region,} \\ \mu_S, & \text{if } \mathbf{r} \in \text{SC region.} \end{cases} \quad (\text{S3})$$

If not stated otherwise, we consider $\mu \equiv \mu_N = \mu_S$. Finally, the s -wave pairing is considered nonzero only in the region proximitized by the SC:

$$\Delta(\mathbf{r}) = \begin{cases} 0, & \text{if } \mathbf{r} \in \text{N region,} \\ \Delta, & \text{if } \mathbf{r} \in \text{SC region.} \end{cases} \quad (\text{S4})$$

Tight-binding description.— The Hamiltonian (S1) is discretized in a square lattice with lattice parameter a as:

$$\begin{aligned} \mathcal{H}_{2\text{D}} = \sum_{i,j} \Psi_{i,j}^\dagger \left([4t - \mu_{i,j}] \sigma_0 \tau_z - \Delta_{i,j} \sigma_z \tau_x + V_{i,j}^z \sigma_z \tau_0 \right) \Psi_{i,j} + \sum_{\langle \text{NN-x} \rangle} \Psi_{i,j}^\dagger \left(-t \sigma_0 \tau_z - i \frac{\alpha_{i,j}}{2a} \sigma_y \tau_0 \right) \Psi_{i+1,j} + \text{H.c.} \\ + \sum_{\langle \text{NN-y} \rangle} \Psi_{i,j}^\dagger e^{-i\tau_z \phi_{i,j}} \left(-t \sigma_0 \tau_z + \frac{i\alpha_{i,j}}{2a} \sigma_x \tau_0 \right) \Psi_{i,j+1} + \text{H.c.}, \end{aligned}$$

where (i, j) indicate the lattice-site indices. The sums in the previous expression are performed over nearest-neighbours (NN) sites in the x and y directions. The hopping term is $t = \hbar^2 / (2ma)$ and the basis used is $\Psi_{i,k_y} = (c_{i,j,\uparrow}, c_{i,j,\downarrow}, c_{i,j,\downarrow}^\dagger, c_{i,j,\uparrow}^\dagger)$.

The vector potential is included through the Peierls phase by replacing the hopping between NN in the y direction by $t_y \rightarrow t_y \exp(-i\tau_z \phi_{i,j})$, with the phase

$$\phi_{i,j} \equiv \frac{e}{\hbar} (\mathbf{r}_{i,j+1} - \mathbf{r}_{i,j}) \frac{\mathbf{A}(\mathbf{r}_{i,j+1}) + \mathbf{A}(\mathbf{r}_{i,j})}{2}. \quad (\text{S5})$$

Here, $\mathbf{r}_{i,j}$ indicates the position of the site with lattice indices (i,j) . The terms $f_{i,j}$, with $f = \{\mu, \Delta, V_z, \alpha\}$, are defined from the continuum functions of the potentials as $f_{i,j} \equiv f(\mathbf{r}_{i,j})$.

The Anderson disorder included in Fig. 5(b) is introduced by defining the chemical potential as

$$\mu(\mathbf{r}) = \begin{cases} \mu_N + w_A \eta(\mathbf{r}), & \text{if } |\mathbf{r} - \mathbf{r}_{\text{NS}}| < d_A, \\ \mu_S + w_A \eta(\mathbf{r}), & \text{if } \mathbf{r} \in \text{SC region}, \\ \mu_N, & \text{otherwise,} \end{cases} \quad (\text{S6})$$

where $\eta(\mathbf{r}) \in [-0.5, 0.5)$ is a uniformly-distributed random value and d_A defines a region near the N-SC interface where a disordered interface is considered.

Details on the numerical calculations and the transport setup.— The transport calculations are performed using `Kwant` [43] in a setup as the one depicted schematically in Fig. 1(a). The leads considered are semi-infinite in the x direction and finite in y direction with a width of $W_{\text{leads}} = 140$ nm. They are described by Eq. (S1) with $\alpha_R = \Delta = V_z = 0$, the chemical potential is fixed at $\mu_L/\Delta = 4.4$.

`Kwant` [43] is employed to extract the scattering matrix \mathcal{S} for a two-lead system as the one sketched in Fig. 1(a). The scattering matrix elements are $\mathcal{S}_{\alpha\beta}^{e,t}$, with α being an electronic (e) incoming mode at the *in* lead and β being an outgoing mode of type $t = e, h$ in the *out* lead. The transmission probability is then obtained by the Landauer-Büttiker formalism at zero-temperature as:

$$T_{\text{CAR}}(E_{\text{inj}}) = \sum_{\alpha,\beta} \left| \mathcal{S}_{\alpha\beta}^{e,h}(E_{\text{inj}}) \right|^2, \quad (\text{S7})$$

$$T_{\text{EC}}(E_{\text{inj}}) = \sum_{\alpha,\beta} \left| \mathcal{S}_{\alpha\beta}^{e,e}(E_{\text{inj}}) \right|^2, \quad (\text{S8})$$

such that the nonlocal conductance is given by

$$G_{\text{nl}}(E_{\text{inj}}) = \frac{e^2}{h} [T_{\text{EC}}(E_{\text{inj}}) - T_{\text{CAR}}(E_{\text{inj}})]. \quad (\text{S9})$$

In the transmission probability results shown in Fig. 2(b) and Fig. 5, the numerical criteria for defining the $E_g \simeq 0$ is set to $E_g/\Delta \leq 0.05$.

The stripe geometry is considered infinite in the y direction and of width $W = 400$ nm in the x direction. In the finger geometry, the calculations in Fig. 3(b) are performed for a system of size $W \times L = 400$ nm \times 600 nm. For the SC island configuration in Fig. 4, the system considered has extension $W \times L = 600$ nm \times 700 nm.

Together with the scattering matrix, the wave function formulation employed in `Kwant` [43] returns as main output the scattering wavefunction $\psi_{s,\alpha}(\mathbf{r})$ that solves the propagation problem of an incoming mode α from lead *in* in the scattering region. In the manuscript, the observables calculated over the scattering wavefunction are defined as

$$\langle \psi_s(\mathbf{r}) \rangle_{\hat{\mathcal{O}}} = \sum_{\alpha} \langle \psi_{s,\alpha}(\mathbf{r}) \rangle_{\hat{\mathcal{O}}},$$

where $\hat{\mathcal{O}}$ denotes the observable operator. In particular, the electron and hole content of the scattering wavefunction represented in Fig. 4 is defined as

$$P_{eh}(\mathbf{r}) = |\psi_s^e(\mathbf{r})|^2 - |\psi_s^h(\mathbf{r})|^2, \quad |\psi_s^t(\mathbf{r})|^2 = \sum_{\alpha} |\langle \psi_{\alpha,s}(\mathbf{r}) \rangle_{\hat{Q}_t}|^2, \quad (\text{S10})$$

with $t = e, h$ and where $\hat{Q}_{e(h)}$ is the projector over the electron (hole) Nambu space.

The local density of states $\rho(\varepsilon)$ represented in the second and third rows of Fig. 4 is defined as:

$$\rho(\varepsilon, \mathbf{r}) = \text{Im} \left[\lim_{\eta \rightarrow 0^+} \sum_m \frac{|\psi_m(\mathbf{r})|^2}{\varepsilon - E_m + i\eta} \right], \quad (\text{S11})$$

where $\psi_m(\mathbf{r})$ is the m -th eigenstate of the system with energy E_m obtained by sparse numerical diagonalization.

EFFECTIVE ANALYTICAL MODEL

Landau levels with RSOC.— In the limit of $\lambda_B = 0$ and $\lambda_z = 0$, the bulk electronic LLs with RSOC are defined by the wavefunctions $\Phi_{e,(n,\chi)}^S$ with energy $E_{(n,\chi)}$, where

$$\Phi_{e,(n,\chi)}^S = \sqrt{(1 + \chi\beta_n)/2} |n, S, \uparrow\rangle + \text{sign}(S) \sqrt{(1 - \chi\beta_n)/2} |n - 1, S, \downarrow\rangle, \quad (\text{S12a})$$

$$E_{(n,\chi)} = \hbar\omega n + \chi \sqrt{(\hbar\omega/2 + V_z)^2 + nE_R^2}, \quad (\text{S12b})$$

with $\beta_n = (\hbar\omega/2 + V_z) / \sqrt{(\hbar\omega/2 + V_z)^2 + nE_R^2}$ and $E_R = \alpha_R \sqrt{2eB_z/\hbar}$ [44, 45]. In these expressions, $\chi = \pm 1$ for $n \geq 1$ and $\chi = 1$ for $n = 0$. The eigenstates $|n, S, \uparrow (\downarrow)\rangle$ represent the spin-polarized n -th LLs with spin direction $\uparrow (\downarrow)$ and localized at the side $S = L, R$. In the following, we use the abbreviated notation in which the lowest-energy state is labelled as $\nu = 1$ and corresponds to the state with $(n, \chi) = (1, -1)$. The state labelled as $\nu = 2$ is given by $(n, \chi) = (0, 1)$. To simplify the notation we also use $\beta \equiv \beta_1$.

Coupling terms.— If we neglect the spatial localization of the LLs in the perpendicular direction to the interface, we can consider the superconducting gap as mainly coupling the spin structure of the LL states. This way, the L-R couplings of the minimal model can be estimated by the following overlap terms:

$$u_0 \sim |\langle \Phi_{e1}^L | \Delta \tau_0 \sigma_0 | \Phi_{e2}^R \rangle| \approx \Delta \beta, \quad (\text{S13a})$$

$$p_0 \sim |\langle \Phi_{e1}^L | \Delta \tau_x \sigma_z | \Phi_{h1}^R \rangle| \approx \Delta \sqrt{1 - \beta^2}, \quad (\text{S13b})$$

$$d_0 \sim |\langle \Phi_{e1}^L | \Delta \tau_0 \sigma_0 | \Phi_{e2}^R \rangle| \approx \Delta \sqrt{(1 - \beta)/2}, \quad (\text{S13c})$$

$$f_0 \sim |\langle \Phi_{e1}^L | \Delta \tau_x \sigma_z | \Phi_{h2}^R \rangle| \approx \Delta \sqrt{(1 + \beta)/2}, \quad (\text{S13d})$$

where Φ_{tv}^S are the bulk LLs localized at side $S = L, R$, of particle type $t = e, h$ and filling factor $\nu = 1, 2$ given by Eq. (S12a). Note that the approximate values for the couplings depend only on the factor β that accounts for the relation of the Zeeman and the Rashba splitting in the bulk LLs.

Conditions for band inversion.— To derive the approximate conditions for $\mathcal{Q}_S = -1$ presented in the manuscript, we use the estimated values for the coupling constants from Eqs. (S13) in the analytical Pfaffian invariant of Eq. (3). In the simplest case of neglecting d , we obtain

$$\mathcal{Q}_S = (-1)^\nu \text{sign} \left\{ \left[E_d^2 + \tilde{\Delta}^2 (\sin^2(k_F W_S) - \beta^2) \right] \left[E_u^2 + \tilde{\Delta}^2 (\sin^2(k_F W_S) - \beta^2) \right] \right\}, \quad (\text{S14})$$

where $\tilde{\Delta} = \Delta e^{-W_S/\xi_S}$. Since $E_d \gtrsim \Delta$ and $0 < \beta \leq 1$, the sign change is only given by the second term and, in particular, its minimal value is obtained for $k_F W_S = n\pi$ with $n = 1, 2, \dots$, i.e., when $p = 0$. This condition fixes the width, such that, by using $k_F \approx \sqrt{2m\mu}/\hbar$ and $\xi_S = (\hbar/\Delta) \sqrt{2\mu/m}$, we obtain

$$\lim_{p,d \rightarrow 0} \mathcal{Q}_S \approx (-1)^\nu \text{sign} \left[E_u^2 - \beta^2 \Delta^2 e^{-n\pi\Delta/\mu} \right], \quad (\text{S15})$$

where, in the following, we only consider the $n = 1$ case.

We can estimate E_u from the subgap expression for the CAESs dispersion from Refs. [19, 20], considering the RSOC as a constant shifting of the bulk bands, namely,

$$E_u \approx 2\Delta \frac{\hbar\omega \pm \Gamma_0 - \sqrt{(\frac{\hbar\omega}{2} + \frac{V_z}{2})^2 + \frac{E_R^2}{2}}}{\hbar\omega/\pi + \Delta}, \quad (\text{S16})$$

where $\Gamma_0 = \frac{\hbar\omega}{2\pi} \arccos(\Omega_0)$, with $\Omega_0 \rightarrow 0$ for an ideal N-QH interface. Assuming that $\hbar\omega \gg E_R > V_z$, we introduce Eq. (S16) in Eq. (S15) and expand it up to second order in E_R around the μ -independent solution $E_R^0 = \sqrt{5/8(\hbar\omega)^2 - V_z(V_z/2 + \hbar\omega)}$. As a result, the condition for $\mathcal{Q}_S = -1$ in Eq. (S15) can be approximated as

$$2\hbar\omega/3 - V_z < E_R < \hbar\omega - V_z/3, \quad (\text{S17})$$

which is further simplified in the text as $2\hbar/3\omega - V_z < E_R \lesssim \hbar\omega$.

In the more general case of considering $d \neq 0$, the condition of band inversion when $p = 0$, i.e., for $k_F W_S = n\pi$, is

$$\lim_{p \rightarrow 0} \mathcal{Q}_S = (-1)^\nu \{ \tilde{\Delta}^4 \beta^4 - \tilde{\Delta}^2 \beta^2 [E_u^2 + E_d^2 - \Delta^2(1 - \beta)] + [E_u E_d - (1 - \beta)\Delta/2]^2 \}, \quad (\text{S18})$$

that leads to a range of E_u given by $E_{lim,-} < E_u < E_{lim,+}$, where

$$E_{lim,\pm} = \frac{(1 - \beta)\Delta^2/2 - \beta^2 \tilde{\Delta}^2 \mp \beta \tilde{\Delta} E_d}{E_d \pm \beta \tilde{\Delta}}. \quad (\text{S19})$$

Without further assumptions on E_u , Eq. (S19) allows us to estimate the values of E_u needed to obtain a band-inversion regime for fixed values of RSOC and Zeeman splitting.

On the other hand, an estimation of the RSOC required to reach $\mathcal{Q}_S = -1$ is obtained in the $d \neq 0$ regime by considering $E_d \approx \Delta$, E_u as in Eq. (S16), and $\hbar\omega \gg E_R > V_z$, leading to the approximate condition

$$\frac{\Delta}{3} + \sqrt{\frac{\hbar\omega}{3}(V_z + \Delta)} \lesssim E_R - \frac{\hbar\omega}{2} \lesssim \frac{\hbar\omega}{3} - \frac{3\Delta^2}{2\hbar\omega}. \quad (\text{S20})$$

Symmetries of the effective model.— The minimal model in Eq. (8) is obtained by imposing the following symmetries:

- Particle-hole symmetry, represented in the basis of the two lowest CAES as $\tilde{C} = \tau_x r_x s_0 \mathcal{K}$ so that

$$\tilde{C} \mathcal{H}_{\text{eff}}(k_y) \tilde{C}^{-1} = -\mathcal{H}_{\text{eff}}(-k_y). \quad (\text{S21})$$

- Magnetic in-plane mirror reflection that relates the Hamiltonian for the L and R sectors in the case of the stripe geometry. In the basis of the minimal model, we represent it as $\tilde{M} = \tau_0 r_z s_x$ and require that

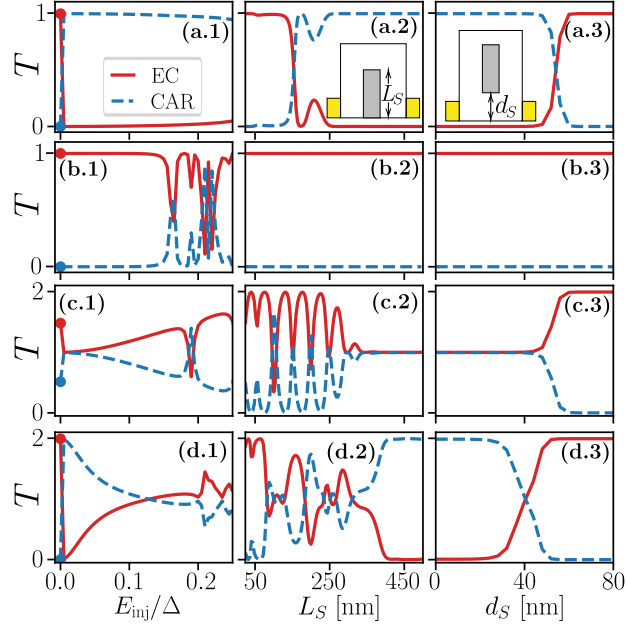
$$\tilde{M} \mathcal{H}_{\text{eff}}(k_y) \tilde{M}^{-1} = \mathcal{H}_{\text{eff}}(-k_y). \quad (\text{S22})$$

- Spin polarization in S_z in the limit of $\alpha_R \rightarrow 0$. In the absence of RSOC, the CAESs are spin-polarized and the spin operator in z commutes with the Hamiltonian, i.e., $[\mathcal{H}_{\text{eff}}, S_z] = 0$, where $S_z = \tau_0 r_z s_0$. This is indeed fulfilled by the effective model for $p \rightarrow 0$ and $d \rightarrow 0$, terms that are only non-zero when including RSOC.

FINITE-SIZE EFFECTS

In this section we briefly discuss finite-size effects on the transport properties for the finger and island configuration, as summarized in Fig. S1. Due to these effects, the transmission probabilities at $E_{\text{inj}} = 0$ do not necessarily reflect the expected quantized values for each topological phase. This can be seen in the first column of Fig. S1 where the energy dependence of the transmission probabilities is represented for the four representative cases discussed in Fig. 4, i.e., for devices with parameters corresponding to a stripe with $\mathcal{Q}_S = \pm 1$ and $\nu = 1, 2$. While the quantized EC in $\nu = 1$ displays no abrupt change at low injection energies [Fig. S1(b.1)], the transmission for $E_{\text{inj}}/\Delta < 10^{-3}$ differs significantly for the other cases involving the appearance of one [Fig. S1(a.1) and Fig. S1(c.1)] or two [Fig. S1(d.1)] CAR channels. Regarding the energy-dependence at higher values, the $\nu = 1$ states are quite more resilient and show perfectly quantized signals up to $E_{\text{inj}} \lesssim 0.2\Delta$.

The second column in Fig. S1 studies the evolution of T_{CAR} and T_{EC} as a function of the length L_S of the SC finger. As expected, the pair of Majorana states formed at each ends of the finger have to be spatially separated to prevent their hybridization, see Fig. S1(a.2), Fig. S1(c.2) and Fig. S1(d.2), and a quantized signal is obtained for $L_S \gtrsim 4\xi_S$. Finally, in column 3, the SC island configuration is studied as a function of the distance d_S defined between the lower end of the SC region and the QH edge, see inset in Fig. S1(a.3). In the limit of $d_S \gg l_B$, the island configuration with SC topological character develops localized Majorana states at the two ends of the SC island, see Fig. 4 panels (i,k,l). By decreasing d_S , the Majorana state localized at the lower edge couples with the LL. As shown in panels Fig. S1(a.3), Fig. S1(c.3) and Fig. S1(d.3) for $d_S \lesssim 2l_B$, i.e., for a separation of the order of the localization of the LL, the localized Majorana state leads to the expected perfect CAR conversion [1, 5]. This way, the hybridized state obtained for $d_S \rightarrow 0$ can be interpreted as a delocalized Majorana state with the same quantized CAR signal.



PHASE DIAGRAMS FOR OTHER SETS OF PARAMETERS

The results presented in the main text and in the End Matter correspond the case of an heterostructure without Fermi level mismatch and with almost perfect magnetic field screening inside the SC region ($\lambda_B = 6$ nm). The phase diagrams are qualitatively similar independently of these conditions, as shown in Fig. S2.

The Fermi level mismatch modifies the evolution of the minigap as a function of W_S and shrinks the topological regions if $\mu_S > \mu_N$, see Fig. S2(a) for a fixed value of $\mu_S/\Delta = 6$. In Fig. S2(b), the case of a broken mirror-symmetric stripe is considered by modifying the chemical potential in only one of the two QH regions setting $\delta\mu = 0.2/\Delta$. Even if the mirror symmetry is protecting the $Q_S = -1$ state, if $\delta\mu < E_g$ the topological phase is still observed. Finally, Fig. S2(c) considers the case of a wider penetration depth of the magnetic field and Zeeman splitting, parametrized by $\lambda_B = 24$ nm. In this case the lowest tongue-like region does not reach $\nu = 1$ for $W_S > \xi_S$. However, a wide range of stripe widths still shows a topological SC gap for higher filling factors.

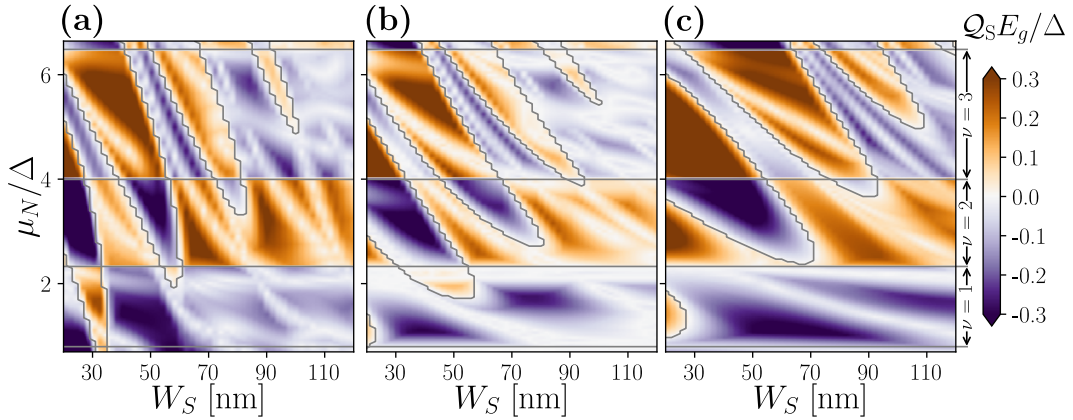


FIG. S2. Phase diagrams for the same stripe configuration as in Fig. 1(a) with: (a) Fermi level mismatch in the SC proximized region given by $\mu_S/\Delta = 6$; (b) Fermi level mismatch in one of the QH regions given by $\mu'_N = \mu_N + \delta\mu$ with $\delta\mu/\Delta = 0.2$; and (c) wider penetration depth of the magnetic field and Zeeman splitting ($\lambda_B = 24$ nm).